

Article

Design and Experimental Tests of a Buoyancy Change Module for Autonomous Underwater Vehicles

J. Falcão Carneiro ^{1,*} , J. Bravo Pinto ² , F. Gomes de Almeida ¹  and N. A. Cruz ³ ¹ INEGI, Faculdade de Engenharia, Universidade do Porto, Rua Dr. Roberto Frias, s/n, 4200-465 Porto, Portugal² Faculdade de Engenharia, Universidade do Porto, Rua Dr. Roberto Frias, 400, 4200-465 Porto, Portugal³ INESC TEC, Faculdade de Engenharia, Universidade do Porto, Rua Dr. Roberto Frias, 4200-465 Porto, Portugal

* Correspondence: jbrfc@fe.up.pt

Abstract: Ocean exploration is of major importance for several reasons, including energy and mineral resource retrieval, sovereignty, and environmental concerns. The use of autonomous underwater vehicles (AUV) has thus been receiving increased attention from the scientific community. In this context, it has been shown that the use of buoyancy change modules (BCMs) can significantly improve the energy efficiency of an AUV. However, the literature regarding the detailed design of these modules is scarce. This paper contributes to this field by describing the development of an electromechanical buoyancy change module prototype to be incorporated into an existing AUV. A detailed description of the constraints and compromises existing in the design of the device components is presented. In addition, the mechanical design of the hull based on FEM simulations is described in detail. The prototype is experimentally tested in a shallow pool where its full functionality is shown. The paper also presents preliminary experimental values of the power consumption of the device and compares them with the ones provided by existing models in the literature.

Keywords: autonomous underwater vehicles; variable buoyancy systems; energy efficiency



Citation: Falcão Carneiro, J.; Bravo Pinto, J.; Gomes de Almeida, F.; Cruz, N.A. Design and Experimental Tests of a Buoyancy Change Module for Autonomous Underwater Vehicles. *Actuators* **2022**, *11*, 254. <https://doi.org/10.3390/act11090254>

Academic Editor: Guanghong Yang

Received: 27 July 2022

Accepted: 1 September 2022

Published: 4 September 2022

Publisher's Note: MDPI stays neutral with regard to jurisdictional claims in published maps and institutional affiliations.



Copyright: © 2022 by the authors. Licensee MDPI, Basel, Switzerland. This article is an open access article distributed under the terms and conditions of the Creative Commons Attribution (CC BY) license (<https://creativecommons.org/licenses/by/4.0/>).

1. Introduction

Oceans are arguably the last unexplored regions on planet Earth. Their importance is widely recognized as a major source of minerals and energy to be explored in the future. During the past decades, researchers from all over the world have started to work on solutions to allow a constant human presence on oceans. Specifically, underwater vehicles have seen major developments as it has been shown that underwater devices are a good solution to circumvent one of the main obstacles found in this field, the survivability of the vehicles. Underwater gliders are perhaps the state-of-the-art example of this effort. An underwater glider can travel long distances (more than 1000 km) for long periods of time (more than one year) while retrieving information on ocean state variables. To achieve this end, underwater gliders travel at low speed, carry low sensor power and use low consumption buoyancy change modules (BCMs). BCMs are also becoming increasingly important as secondary engines for thruster-powered devices in hybrid AUVs [1–4]. In fact, the use of BCMs in thruster-based vehicles has numerous benefits, as it allows hovering tasks with small energy consumption, automatic ballast and trim. It also allows the angle of attack of the vehicle in horizontal motion to be reduced, thus reducing drag and increasing horizontal propeller efficiency [5]. Moreover, it has been recently shown [6] that the use of BCMs is significantly beneficial in hovering tasks compared to the use of vertical propellers, even for relatively small depths and mission lengths. The use of BCMs has, however, some drawbacks, namely regarding the maneuverability of the vehicle. To this end, an innovative underwater glider was developed in [7] which includes an efficiently actuated caudal fin with bidirectional turning capabilities.

It is possible to find very different BCMs in the literature. The most common ones are linear electric drives using seawater as working fluid [8–12] and hydraulic pumping systems [13–16]. A description of more particular solutions involving the use of pneumatic, thermal and hybrid solutions can be found in [6,17]. Hydraulic solutions typically lead to more compact devices than exclusively electric ones but are, however, less efficient at shallower depths (up to 100 m) due to the high relative weight of mechanical friction losses at low pressures [6]. Since the range of depths considered in this work are shallow waters, this paper will be focused on solely electric-based solutions. This choice is further justified by the fact that commercially available linear electromechanical actuators present a large range of forces, with compact solutions incorporating the mechanical transmission and rotational to linear motion conversion. This makes the overall solution very simple from a conceptual point of view, with a linear electric drive driving a piston which moves seawater inside and outside the vehicle, thus changing its buoyancy. Several examples of this solution can be found in the literature. For instance, in [8], an electric drive is used to extend or retract a metallic bellow in a cable-connected BCM to be used in applications such as payload positioning, sensors or communication modules. A mathematical model of the BCM is developed in [8] to simulate the behaviour of the system and predict the time that the device takes to travel between depths. These systems have a nonlinear behaviour which is hard to control using linear controllers. To cope with this, the work in [8] was further expanded in [9] by testing different nonlinear depth controllers. Experimental tests were performed in [10], with two BCMs assembled in opposite directions. The use of metallic bellows in BCMs is nevertheless typically limited by the maximum pressure allowed; thus only small depths can be achieved by this technological solution. In [12], a stepper motor was used to drive a piston connected to a diaphragm that is able to dive to depths up to 20 m. The buoyancy engine is fitted into a 1 m long, 10 cm wide ABS pipe, but no experimental results are presented.

Arguably, the most tested BCMs are the ones equipping the Slocum gliders. The technological solution of the shallow versions of the BCM used in these vehicles—a linear actuator moving a rolling diaphragm piston—is similar to the one followed in this work. For instance, in the G2 Slocum glider, a single-acting piston design that uses a 90-watt electric motor and a rolling diaphragm sealed piston moves 460 cc of sea water directly into and out of a port on the glider nose centreline [18]. The maximum depth achieved by these devices is either 30, 100 or 200 m, depending on the type of gearbox used in the motor.

Unfortunately, few studies in the literature present details on the mechanical and actuator design in the field of buoyancy change modules. From the studies found in the literature using electromechanical actuators pumping seawater, just a few details on the mechanical design and choice of the actuators are presented in [8]. Studies [9,10] are mostly focused on the modelling and control of the linear actuator, while study [11] is mostly focused on the model and experimental trials of the buoyancy engine. In [12], some technological insights on the development of the variable buoyancy engine are given, but information on the several design choices is more based on a trial-and-error basis than on informative choices. Some design details can also be found on hydraulic-based buoyancy devices, but since these devices are mainly aimed at deep sea vehicles, they are not directly comparable with the solution devised in this work. For instance, in [14] an hydraulic buoyancy engine is developed that is able to reach more than a 3000 m depth. Some details on the electric motor of the piston pump and on the hydraulic valve used are provided; however, no design insights on the reasons driving those choices are presented. In summary, none of the above-presented studies provides specific details on the mechanical development of the hull or on an informative choice of the components of the actuation devices, so the design process for BCMs is not known in full [19].

This paper tries to fill this gap by presenting a detailed description of the constraints and compromises existing in the design of buoyancy change modules. Namely, the choice of the device components is discussed, and the mechanical design of the hull based on FEM simulations is described in detail. Since the literature provides little information on these

aspects, it is expected that the contents of this paper might contribute to help researchers in future development of similar modules.

Preliminary tests enabling the experimental characterization of the engine are also provided, with experimentally measured power and energy consumptions. These values are compared with the ones provided by models that were recently presented in the literature by the authors. Since power consumption is critical in autonomous underwater vehicles, as it directly affects the mission length, it is believed that the contents of this paper, which are of utmost importance regarding the energy efficiency of buoyancy change modules, may contribute to more informative future development of these devices.

The paper is organized as follows: Section 2 briefly describes the AUV in which the BCM developed in this work will be installed. Based on that description, the generic requirements for the BCM considered in this study are presented. Next, Section 3 presents the mechanical design of the BCM. Section 4 presents the experimental values obtained with the developed BCM and a comparison with the ones predicted. Finally, Section 5 summarizes the main conclusions obtained from this work.

2. Materials and Methods

2.1. AUV Description

The BCM developed in this work will be installed in small-size AUVs based on modular building block previously developed by one of the authors of this work [20]. The vehicle hull is composed of modular sections with an outer diameter of 200 mm. These blocks can be interchanged, removed, or swapped, possibly varying the overall length, while keeping the cylindrical profile. The MARES AUV was the first vehicle built using this modular building concept in 2007 [21]. It is a portable AUV weighing approximately 35 kg, designed for operations up to 100 m of depth—please check Figure 1.



Figure 1. MARES AUV built using modular components.

One of the unique features of MARES is that it has no control surfaces (i.e., fins). The usual configuration uses two independent horizontal thrusters to control surge and yaw and two through-hull vertical thrusters to control depth and pitch. This allows the AUV to hover in the water column in tasks such as close range inspection of any structure. For safety reasons, it is usual to trim the vehicles with a little positive buoyancy so they may resurface in case of failure or in the presence of significant changes in water density. This means that extra flotation must be imposed on the vehicle, causing the thrusters to deliver a significant amount of power to maintain a given depth. This problem becomes even more significant in missions requiring the vehicle to spend long times in hovering tasks. By coupling the BCM developed in this work to the MARES vehicle, it is expected that significant energy savings might be obtained in specific missions. Table 1 lists some significant characteristics of the MARES AUV that are relevant for this work. More specific details can be found in [6].

Table 1. Main characteristics of the MARES AUV.

Power required to remain at same depth	19.8 W
Power required to travel at a descending vertical speed of $\dot{z} = 0.2 \text{ ms}^{-1}$	38 W
Depth Rating	100 m
Endurance	10 h \approx 50 km

2.2. Buoyancy Change Module Requirements

The BCM developed in this work was designed under the modularity concept described above. It is meant as a first step towards the development of two buoyancy modules to couple to the MARES vehicles, one at the stern and one at the bow of the vehicle. Each BCM in MARES/DART should meet the following requirements (please check [6] for further details):

1. Starting from a neutral state, a total volume change of approximately $\pm D_t = \pm 350 \text{ cm}^3$ should be ensured;
2. Its components should fit inside a cylinder with an outer diameter of 200 mm and an inner diameter of 180 mm (the inner diameter of the Mares vehicle);
3. The BCM should have a buoyancy as close as possible to zero at its neutral state;
4. The BCM should withstand a 1 MPa external pressure, corresponding to a depth of 100 m;
5. A volume variation of 700 cm^3 should be achieved in a maximum time close to $t_{vbs} = 30 \text{ s}$;
6. The system should operate from the AUV internal power system at 14 VDC.

3. Mechanical Design of the Buoyancy Change Module

A major guideline underlying the solutions presented in this section is to use, as much as possible, off-the-shelf solutions. This is because it is believed that this strategy might lead to a simpler and faster mechanical design. It was also tried, as much as possible, to avoid the contact of metallic parts with seawater, as this reduces corrosion problems. Furthermore, all elements that must contact seawater were chosen to be as easily replaceable as possible.

3.1. General Description

The solution studied in this work was developed on the working concept shown in Figure 2 and presented in [6]. It includes an electric motor, a transmission and a spindle that drives a piston in and out, thereby altering the volume of the AUV. To avoid leakages in sealing, a rolling diaphragm piston was used. This solution has the additional advantage of neglectable friction forces, therefore reducing power losses and the need for complex position control.

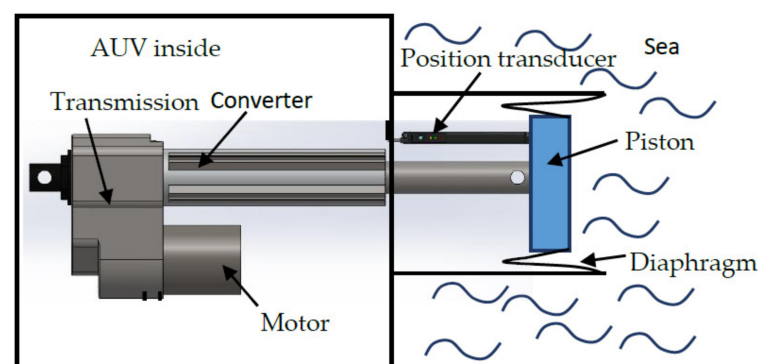
**Figure 2.** Generic principle of the electromechanical solution.

Figure 3 shows a 3D rendering of the cross section and an exploded view of the BCM developed in this work.

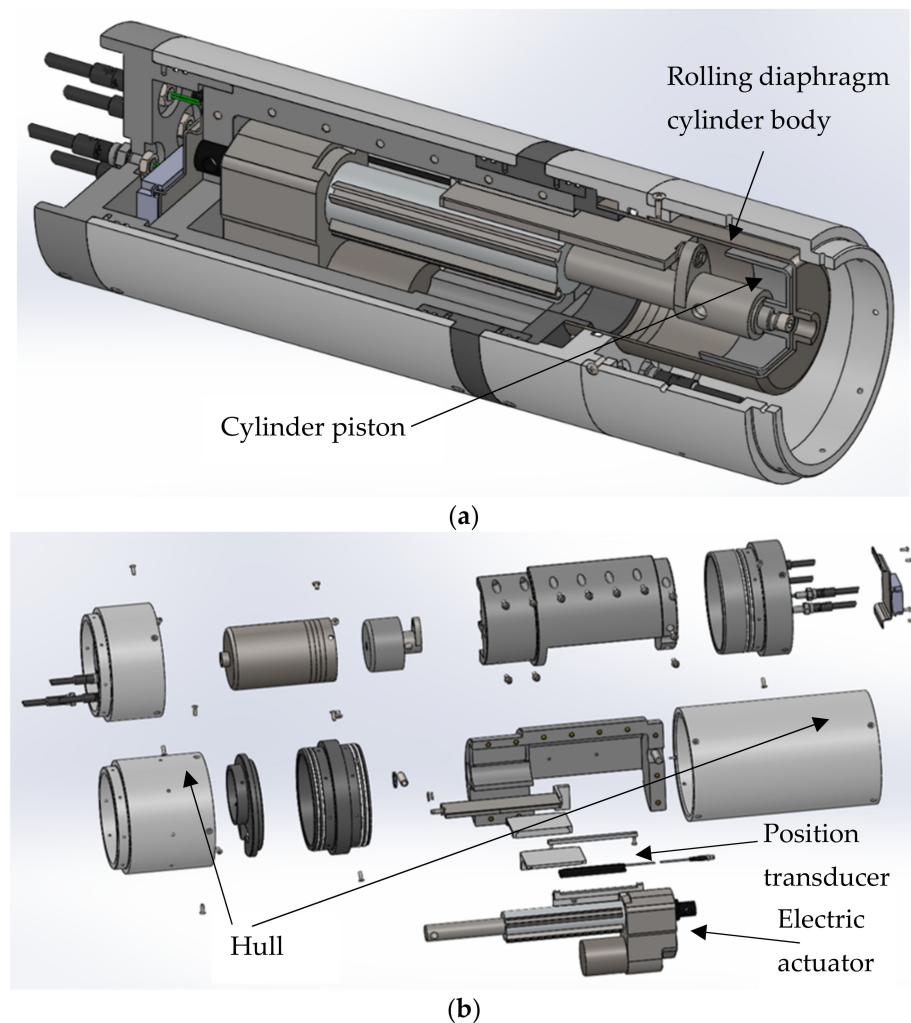


Figure 3. (a) 3D rendering of the cross section of the BCM; (b) exploded view.

In Figure 3, it is possible to distinguish among other elements the hull, made from a polyoxymethylene (POM) tube, the electric actuator and the rolling diaphragm cylinder. The measurement of the piston position, enabling the computation of the displaced seawater volume, is performed by a FESTO SDAT-MHS-M100-1L-SA-E-0,3-M8 transducer. This transducer measures the displacement of a magnet which is mechanically coupled with the piston position. The absence of mechanical contact contributes to the longevity of the measurement system. To accomplish the force and volume displacement requirements defined in the previous section, the sizing of the rolling diaphragm cylinder was made trying to achieve a good compromise between stroke and piston area. Large strokes are undesirable as they increase the length of the vehicle, while large piston areas are also undesirable as they require a higher electric actuator load capacity. The next sections detail the compromise achieved in this work between these two conflictive requirements.

3.2. Sizing of the Rolling Diaphragm Cylinder

Rolling diaphragm cylinders are not as ubiquitous as their ring-sealed counterparts, so there are not many off-the-shelf rolling diaphragm cylinders available on the market. Controlair Inc. is one major supplier for this type of cylinder and offers a limited range of stroke and piston diameter combinations. Table 2 presents some of those options leading to a displaced volume close to 700 cm³. All cylinders presented in this table enable a maximum pressure of 1 MPa, therefore complying with the depth requirements detailed in Section 2.2.

Table 2. Controlair actuator available dimensions.

Piston Diameter [in]	Stroke [in]	Piston Diameter [mm]	Piston Area [mm ²]	Stroke [mm]	Volume [cm ³]	Required Force @1 MPa [N]
3.4	3	86.36	5857.5	76.2	446.34	5858
3.9	2.3	99.06	7707.0	58.42	450.24	7707
3.9	3.6	99.06	7707.0	91.44	704.73	7707
4.5	2.6	114.3	10,260.8	66.04	677.62	10,261
4.5	4.2	114.3	10,260.8	106.68	1094.62	10,261

Based on these options, a cylinder with a piston diameter of 3.9 inches and a 3.6 inches stroke was chosen. The specific model is a single acting SL-12-L. This option is justified by the fact that it leads to a displaced volume of 704.7 cm³ while ensuring that the required force is lower than the one required with a piston diameter of 4.5 inches.

3.3. Sizing of the Linear Actuator

A review of the available market products using electric solutions providing linear motion was performed to achieve the force and stroke required by the cylinder chosen in the previous section. For compactness reasons, solutions including an electric motor, a transmission and a rotation to linear motion converter were considered. Typically, the transmission is a synchronous belt, while the converter is a screw. Additional conditions to be met by the actuator are: (i) to be compatible with a power supply of 14 VDC, avoiding the energy inefficiency associated with DC/DC converters, (ii) comprising a brake which is activated whenever energy is switched off, (iii) to have a stroke compatible with the one determined in the last section, and (iv) to have the best possible overall efficiency.

Table 3 presents some of the options available on the market complying with these requirements. It should be noted that the Thomson actuator, although having a nominal voltage supply compatible with the power supply used in this work, does not allow the use of PWM for speed regulation. Since at nominal voltage the speeds attained would be higher than the target one, it has been discarded from further comparisons.

Table 3. Different linear electric actuators initially considered in this work.

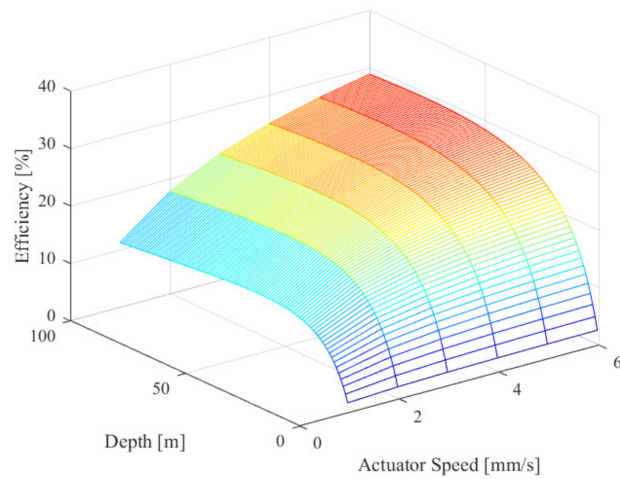
Manufacturer	Model	Stroke [mm]	Maximum Force [N]	Nominal Voltage [V]
Warner Linear	B-Track K2XG30-24VDC	100	12,455	24
Warner Linear	B-Track K2XG30-12VDC	100	12,455	12
Linak	LA 37 12VDC	100	15,000	12
Thomson	HDB 160 12VDC	100	15,000	12

In order to compare the Warner Linear and the Linak actuators, the efficiency of the electromechanical converter (η_{em1}) required by these actuators under different pressures was determined, using the models obtained in [6]:

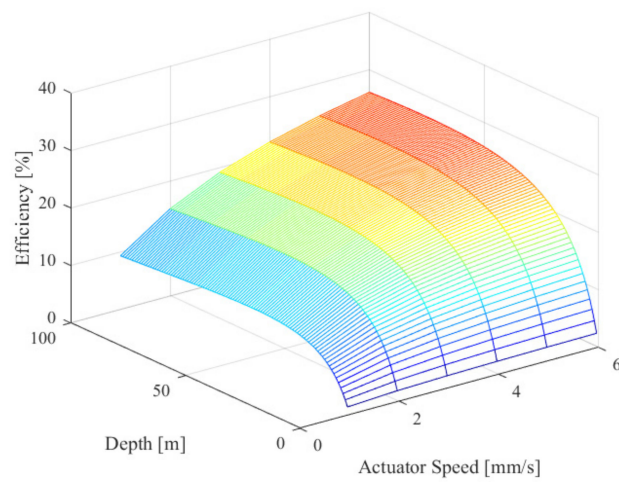
$$\eta_{em1} = \frac{F_{con_t} \times v_{con_t}}{V_t \times I_t} \quad (1)$$

In Equation (1), F_{con_t} is the target force at the mechanical converter output, v_{con_t} is the target velocity at the mechanical converter output, V_t is the target voltage at the driver input, and I_t is the target current at the driver input.

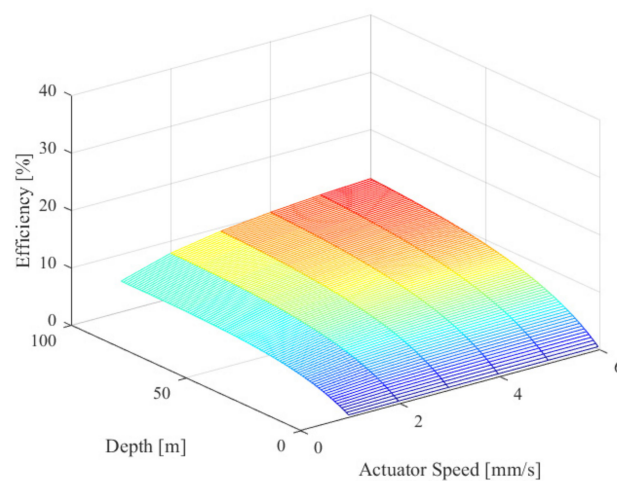
Figure 4 shows a comparison between the efficiencies of the adequate actuators presented in Table 3, assuming that the driver losses are similar to the ones considered in [6].



(a)



(b)



(c)

Figure 4. Energy efficiency at different depths and actuator speeds for: (a) Warner Linear 24VDC; (b) Warner Linear 12VDC; (c) Linak.

The efficiencies presented in Figure 4 were computed using Equation (1), for different target depths and for target speeds around the required in this application (speeds around

3 mm/s). This speed was calculated to comply with Requirement 5 of Section 2.2 and for the stroke of the rolling diaphragm actuator chosen in Section 3.2. As can be seen in Figure 4, for the range of forces and velocities of this application, the Linak actuator is far less efficient than the other two and is thus discarded. Comparing the 12 V and the 24 V Warner Linear actuators, the 24 V version has a slightly better efficiency and was thus the actuator used in this work.

3.4. Sizing of the Structure

The structure of the AUV must withstand mechanical stress due to two main causes. First, since the linear actuator does not contain an anti-rotation system, an external one must be devised to prevent the rod from rotating. Otherwise, the actuator would not be able to withstand the external force caused by the pressure of the sea on the diaphragm cylinder. Second, the BCM hull must withstand the pressure caused by the depth at which the module travels.

3.4.1. Sizing of the Linear Actuator Torque

To generate force in the motion direction, the actuator rod produces a torque which needs to be supported. To absorb that torque, the structure shown in Figure 5 (structure 1) was devised. The rod transmits said torque through the coupling to the steel guide which travels along the sliding element. The stress is then transferred to Structure 1 which is connected to the back of the actuator through the support pin, thus containing the effects of the actuator torque.

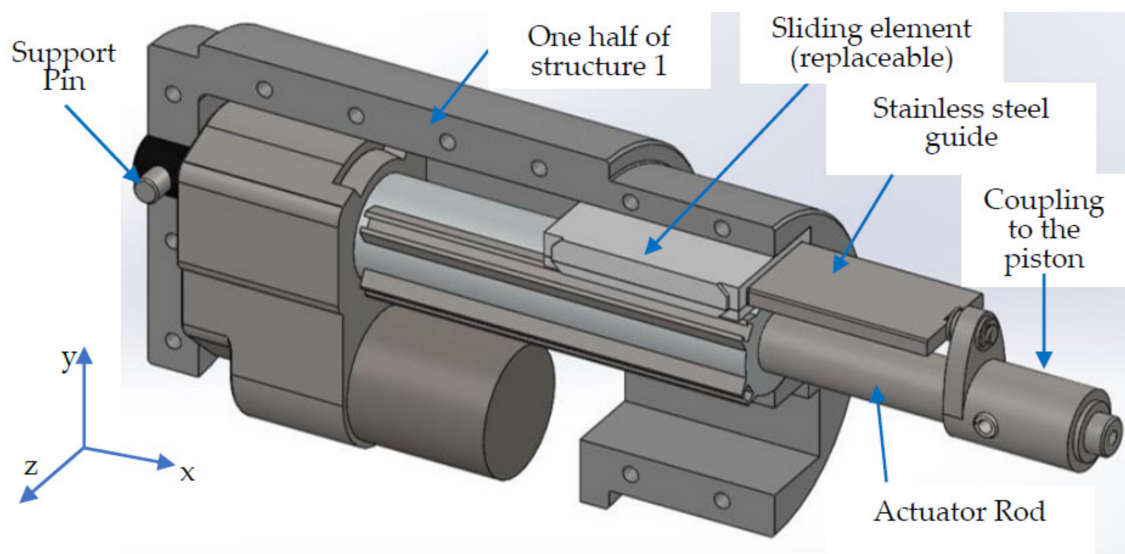


Figure 5. Detail of the structure designed to withstand the torque created by the actuator rod.

Structure 1 is made of POM and was devised to fit into the hull tube while accommodating the linear actuator inside. For this reason, this structure cannot be completely closed, as the motor occupies a considerable space below the spindle. In addition, for the actuator to be assembled, this structure is divided into two halves, only one of which can be seen in Figure 5.

The maximum torque developed by the actuator rod is 11.3 N.m. This means that the force transmitted by the guide to the structure is 323 N, given the distance between the rod and guide centres (35 mm). This distance was designed to be as far as possible to reduce the transmitted force. Since the lateral area of the guide is $A_g = 800 \text{ mm}^2$, a maximum pressure of $p_g = 403,750 \text{ N/m}^2 = 0.4 \text{ MPa}$ is exerted on the guidance area. The maximum velocity at which the actuator travels is 3 mm/s, so the product $p_g \times v_g$ is $1211 \text{ Pa} \times \text{m} \times \text{s}^{-1}$. For POM material, the maximum $p_g \times v_g$ value is $94,500 \text{ Pa} \times \text{m} \times \text{s}^{-1}$ [22], so no guidance wear problems are foreseen. In addition, the sliding element was designed to be replaceable

so that if any wear occurs, it can be changed. To show the effect that the rod torque has on the several elements that must absorb it, FEM simulations were performed using SolidWorks. To perform these simulations, presented in Figures 6–9, a few restrictions were considered: the support pin was fixed in place, the coupling and Structure 1 shown in Figure 5. could only rotate around their cylindrical face axis and the tip of the steel guide could not move along the X direction. As can be seen in Figure 6, the maximum total displacement occurs at the tip of the coupling when the rod is extended and has a value of 0.65 mm. However, this value is not critical since it does not mechanically influence the module in any way. The critical point to be considered is on the inside end of the steel guide (see Figure 7), where the magnet for position measurement is located. In fact, if this part of the steel guide suffers significant displacement on the X direction due to the torque applied by the actuator, the piston position measurements might be compromised. As such, Figure 7 shows the X displacement produced by the actuator torque. From Figure 7, it is possible to see that the X displacement value for the magnet inside end of the steel guide is 0.041 mm when the rod is extended and 0.013 mm when the rod is retracted, meaning that there is very little influence on the position read by the transducer due to the steel guide deformation.

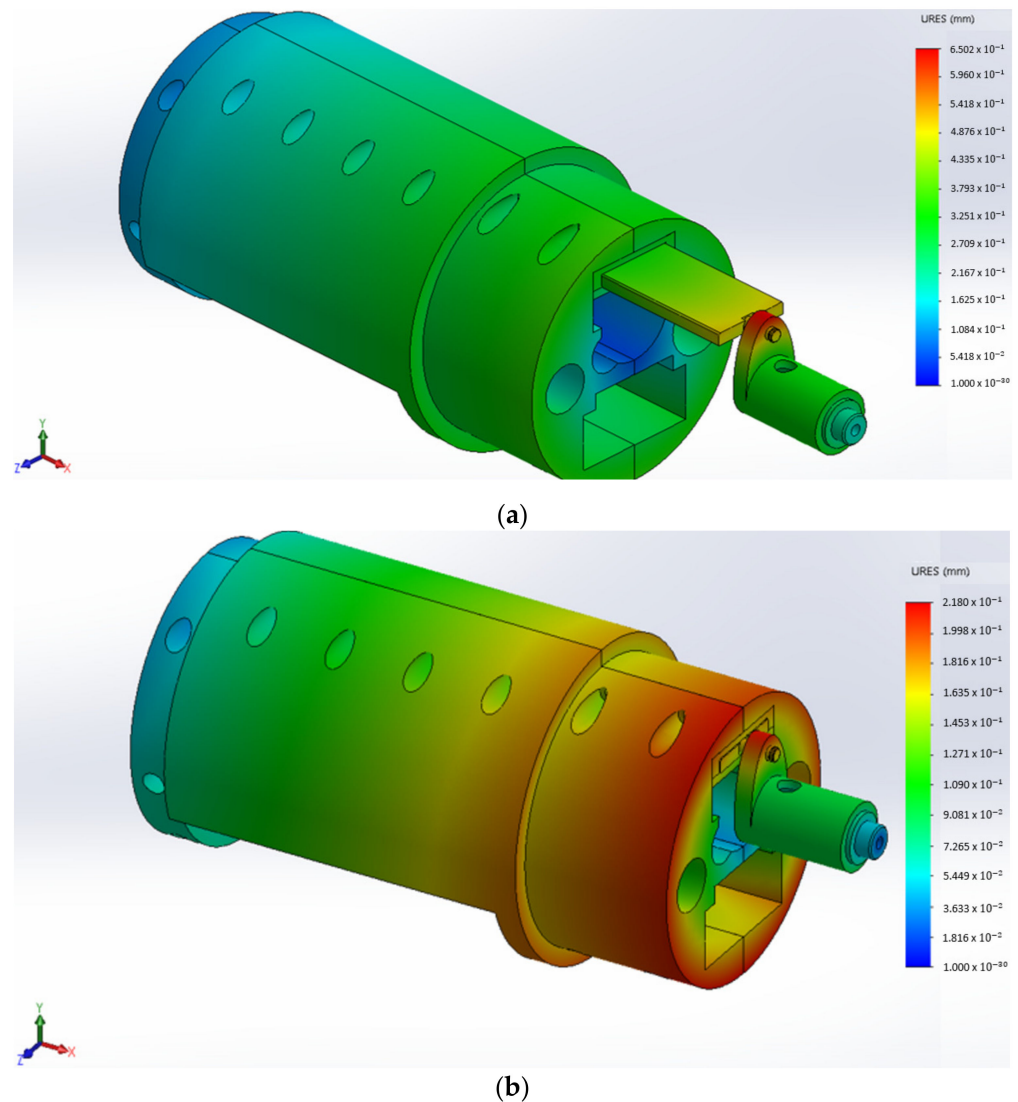
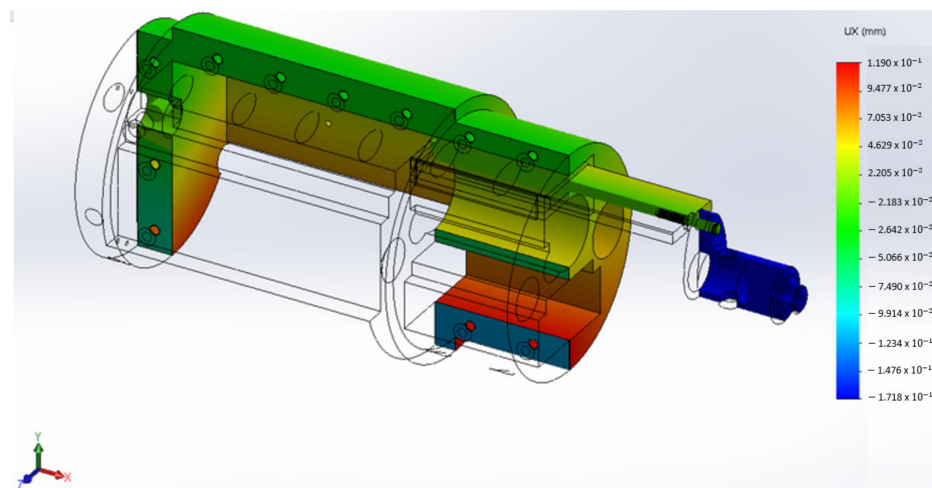
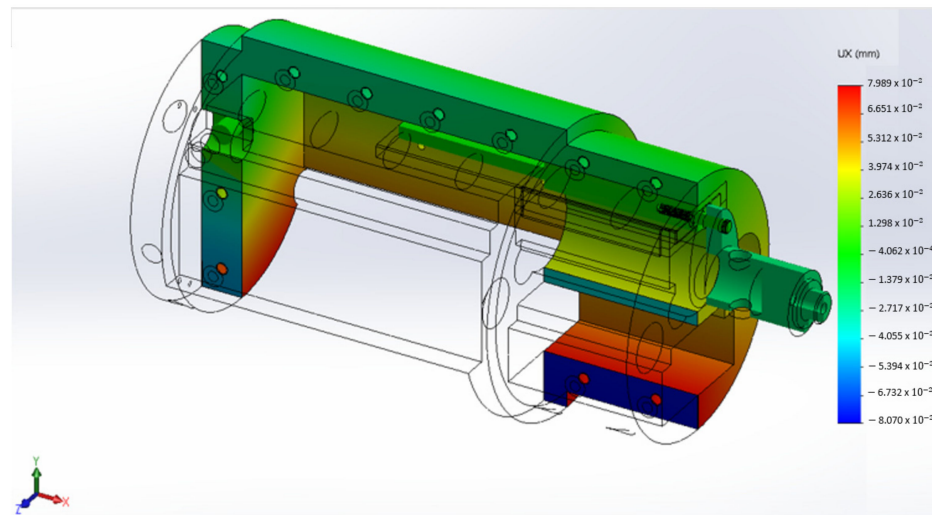


Figure 6. Total displacement when the rod is: (a) extended; (b) retracted.

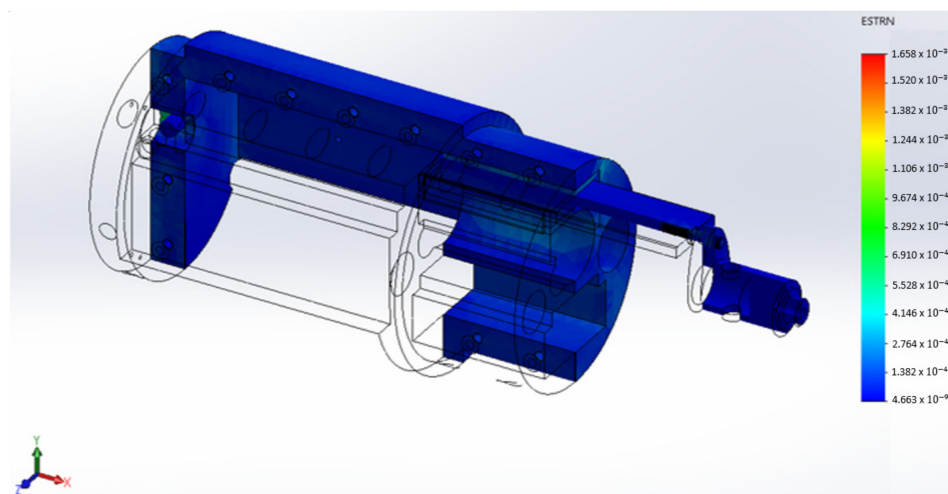


(a)



(b)

Figure 7. Displacement at X direction on the guiding element when the rod is: (a) extended; (b) retracted.



(a)

Figure 8. Cont.

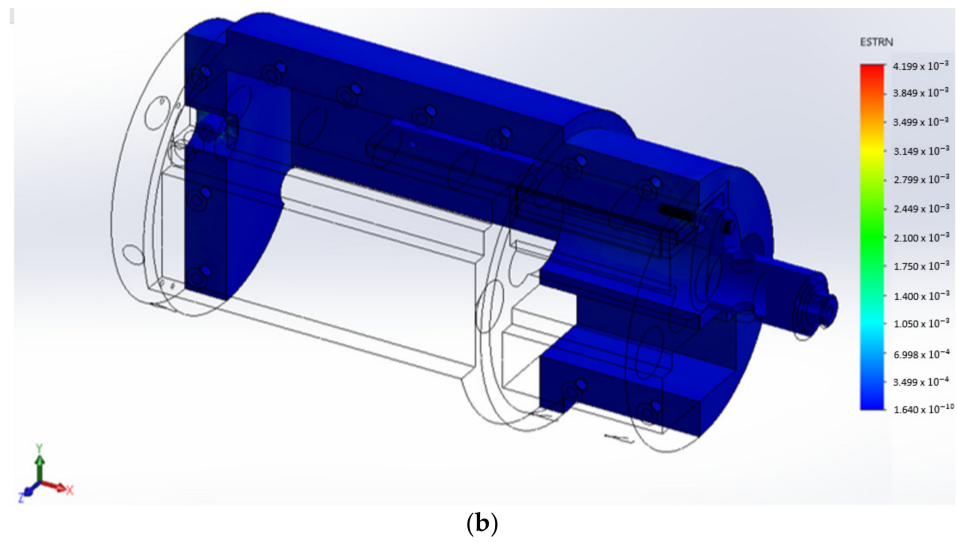


Figure 8. Strain FEM simulation when the maximum torque is exerted by the actuator rod: (a) extended; (b) retracted.

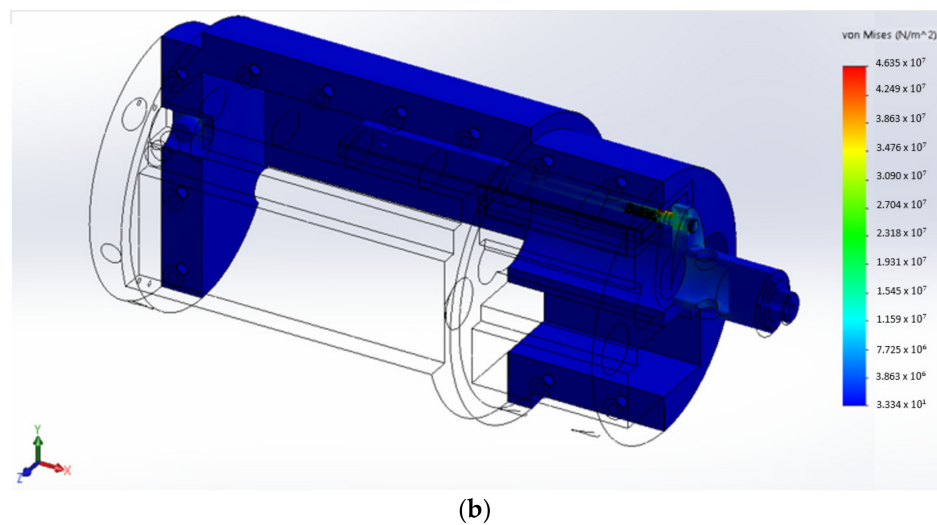
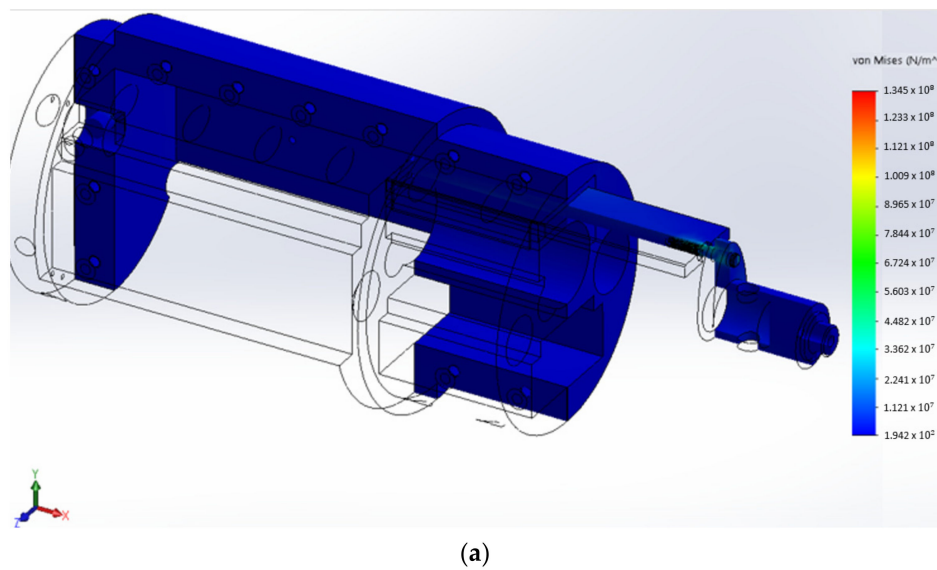


Figure 9. Stress FEM simulation when the maximum torque is exerted by the actuator rod: (a) extended; (b) retracted.

Regarding the stress and strain simulations, it is important to mention that usually a stress-based criterion is used for sizing metal parts. However, since for similar stress values the strain in POM is much bigger and could result in problems disassembling the BCM, the elongation at yield was the criterion used to check if the POM sizing is adequate. To this end, Figures 8 and 9 present the FEM results of strain and stress results, respectively.

As can be seen in Figure 8, the maximum strain is 0.42%, which is very low compared to the 9% elongation at yield of POM. Figure 9 shows the stress produced by the actuator torque, with a maximum value of 134.5 MPa at the tip of the guiding rod. This value is considerably below the maximum stress allowable for 304 Steel (206.8 MPa), so no problems are foreseen.

3.4.2. Simulation of the Sea Pressure Effects on the Structure

The second effort that the BCM must withstand is the one caused by the external pressure of the sea water, which increases with depth up to a maximum value of 10 bar (corresponding to a maximum 100 m dive depth). To simulate the mechanical state of the BCM in this situation, all non-structural parts of the BCM were removed, and a piston was used to simulate the effect of the water on the electric actuator supporting pin. An outside pressure of 10 bar, acting on the outside part of the hull and on the piston, was then applied (red arrows in Figure 10). For the simulation to run, the edges highlighted with green arrows in Figure 10 were kept fixed. Results shown in Figure 10 show that a maximum strain of 1.64% was produced at the hole where the pin supporting the actuator is held in place. This value is well below the 9% elongation at yield of POM, so no critical mechanical problems are foreseen caused by the sea pressure.

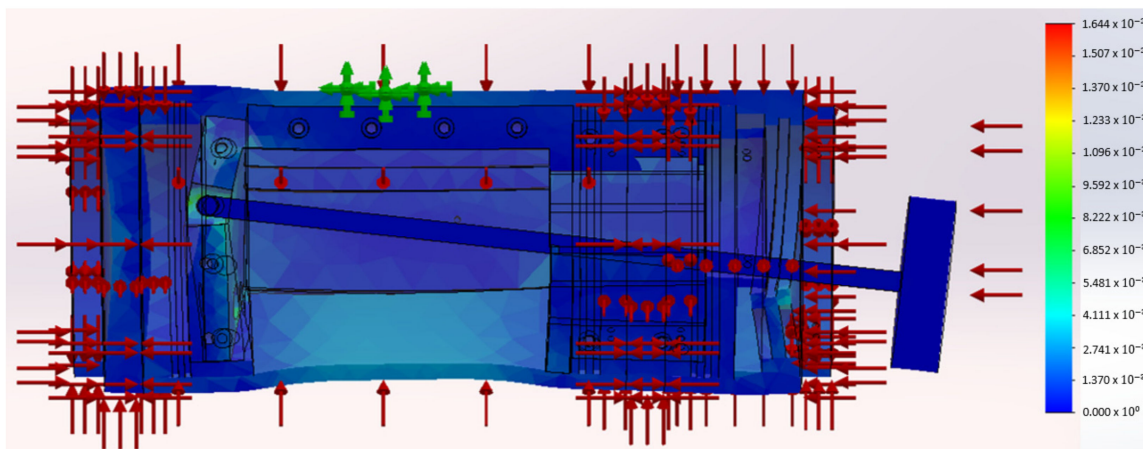


Figure 10. FEM simulation strain results of the sea pressure on the BCM structure.

3.4.3. Simulation of the Sea Pressure on the Body of the Rolling Diaphragm Cylinder

The rolling diaphragm cylinder is where the buoyancy change of the module will occur. Even though the rolling diaphragm cylinder is prepared to withstand 10 bar pressure from the inside, a FEM analysis of the cylinder body was performed to ensure that the cylinder would not fail due to stress or buckling due to the 10 bar outside pressure. The worst working situation is when the buoyancy is at its maximum. In this case, there is a 10 bar pressure on the outside of the length of the cylinder body and no pressure on the inside. For these FEM simulations, presented in Figures 11 and 12, it was considered that the cylinder was connected with screws to a POM part which was also considered to be fixed. In addition, the outside pressure was applied on the cylinder body up to the place where the O-ring seals the module. Figure 11 shows that the maximum stress is 20 MPa, indicating that failure will not occur from the stress generated by the sea pressure, as this stress is well below the maximum stress for steel. Figure 12 shows the shape of the deformation should the cylinder fail due to buckling. For buckling not to occur, the

Buckling Factor of Safety should be bigger than one. In this case, the value obtained through the FEM simulation is 63.71, which means that no buckling is foreseen.

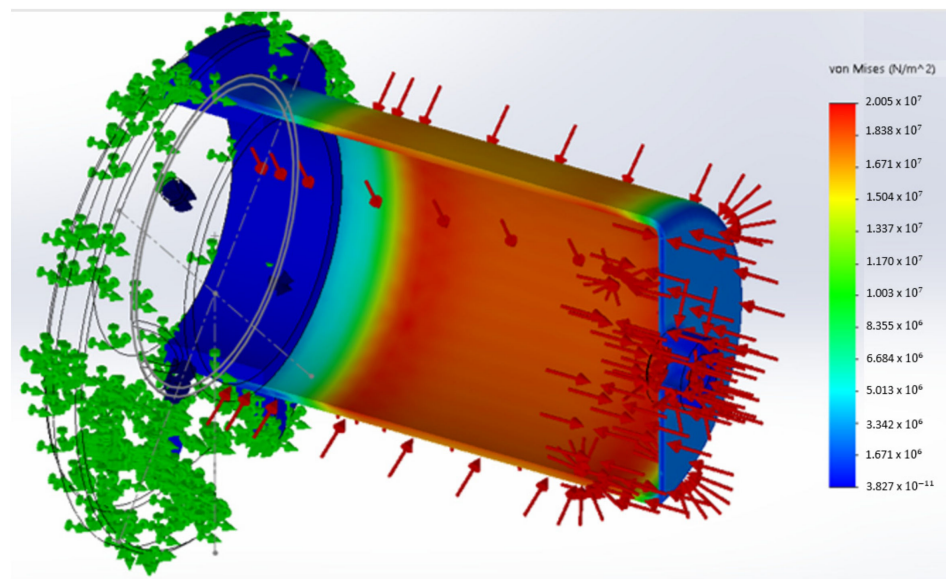


Figure 11. FEM simulation of the sea pressure on the rolling diaphragm cylinder—stress results.

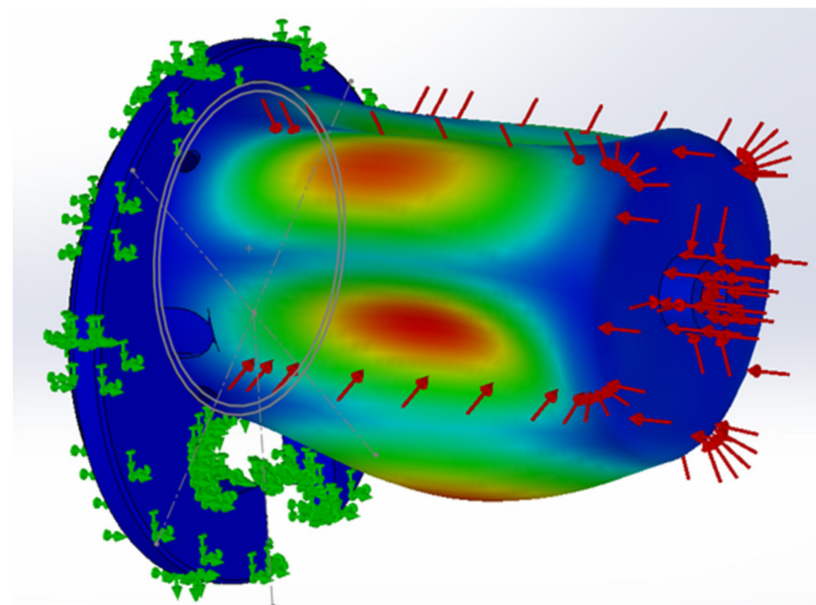


Figure 12. FEM simulation of the sea pressure on the rolling diaphragm cylinder—buckling shape.

4. Power and Efficiency Experimental Results

4.1. Developed Prototype

Figure 13 shows pictures of the developed prototype in several situations. Figure 13a shows the complete BCM, Figure 13b shows the BCM without the front cover, Figure 13c,d show the BCM without the cylinder body and membrane in both retracted and extended positions, respectively. The dashed line in Figure 13a indicates the reference 0 m depth considered in Section 4.4.

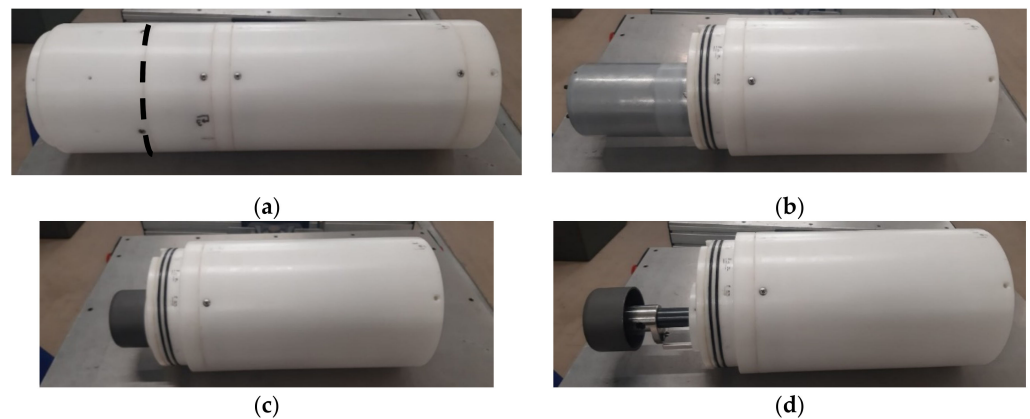


Figure 13. Developed prototype: (a) complete; (b) without front cap; (c) without front cap and cylinder body, retracted; (d) without front cap and cylinder body, extended.

4.2. Measurement and Control Architecture

The control architecture of the system is depicted in Figure 14. The driver of the DC motor (Roboclaw 2x15A) receives the information of the position transducer and is responsible for modulating the voltage applied to the motor using Pulse Width Modulation. The main control unit, implemented with an Arduino Uno, is responsible for delivering to the driver the actuator target positions and recording the information retrieved by the driver (battery voltage, PWM percentage, current, temperature, etc.).

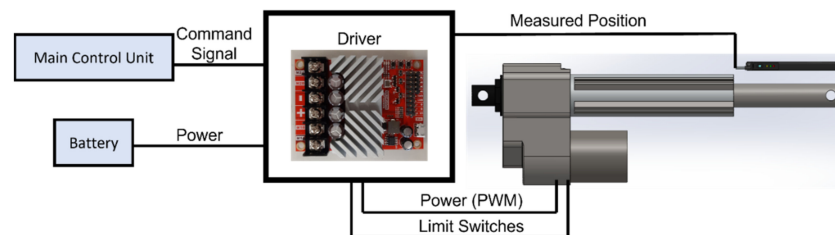


Figure 14. Control architecture.

The position transducer has a resolution of $50\ \mu\text{m}$. Given the area of the rolling diaphragm cylinder, this corresponds to a theoretical volume displacement resolution of $0.38535\ \text{cm}^3$. However, when implementing the system, a dead band of $\pm 500\ \mu\text{m}$ was required to avoid measurement noise. Consequently, the practical displacement resolution is limited to $\pm 3.8535\ \text{cm}^3$, corresponding to a resolution of ca. $\pm 0.5\%$ of the total displacement.

4.3. Vacuum Measurements

Before being inserted into water, a vacuum test on the inside of the BCM was made to ensure that the sealing was efficient. Two different tests were conducted, each one at an average value of approximately 0.3 bar and approximately 0.5 bar. In Test 1, the pressure inside the BCM was measured during approximately 5 min around the middle and the two extreme positions. In Test 2, the pressure was measured for 15 min around the middle position. The pressure was measured using a Druck PTX 1400 transducer. Results, shown in Figure 15, show that for Test 1 there is a slight increase in pressure whenever the position of the actuator is decreased, while for the same position there is not any significant decrease in pressure over time, even for long time. The slight increase in pressure whenever the actuator position is decreased is expected since the internal volume of the BCM is reduced. To ensure that the rolling diaphragm is always held against the piston, a slight vacuum (≈ 0.75 bar absolute pressure) was imposed inside the BCM during the tests presented in Section 4.4 unless stated otherwise.

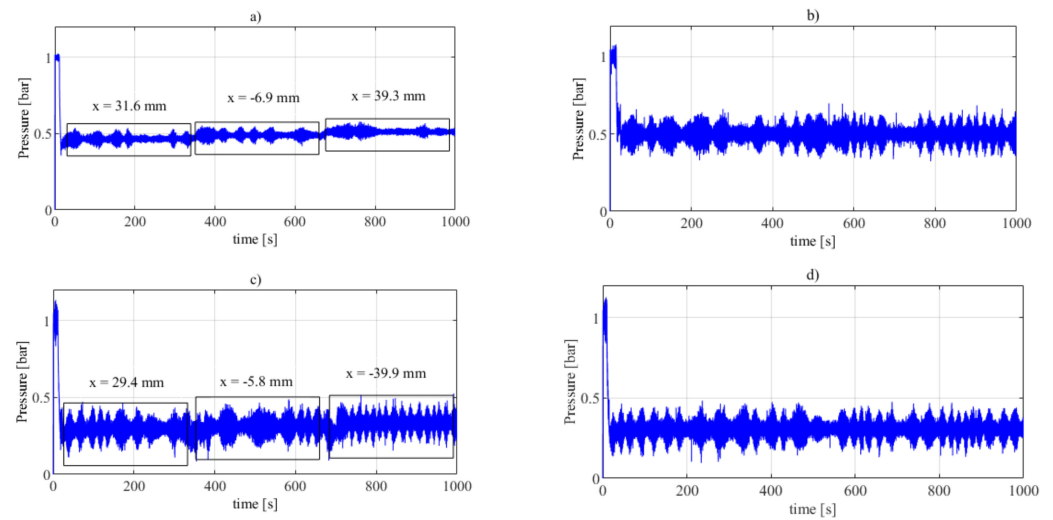


Figure 15. Vacuum measurements inside the BCM hull: (a) test 1 @0.5 bar; (b) test 2 @0.5 bar; (c) test 1 @0.3 bar; (d) test 2 @0.3 bar.

4.4. Experiment in Water Measurements

The experimental setup used to characterize the BCM is presented in Figure 16. It includes a 1.8 m depth pool inside which a dynamometer suspends the BCM. The dynamometer (a portable electronic scale) has a resolution of 10 g. In the trials conducted in this study, the buoyancy of the BCM was intentionally kept negative so that the device always had a tendency to dive. By measuring the weight on water of the BCM for different positions of the diaphragm cylinder and at different depths, along with the corresponding voltage and current drawn by the driver, an experimental assessment of the useful volume change and power consumption achieved by the device was obtained. The 0 m reference is indicated in Figure 13a.

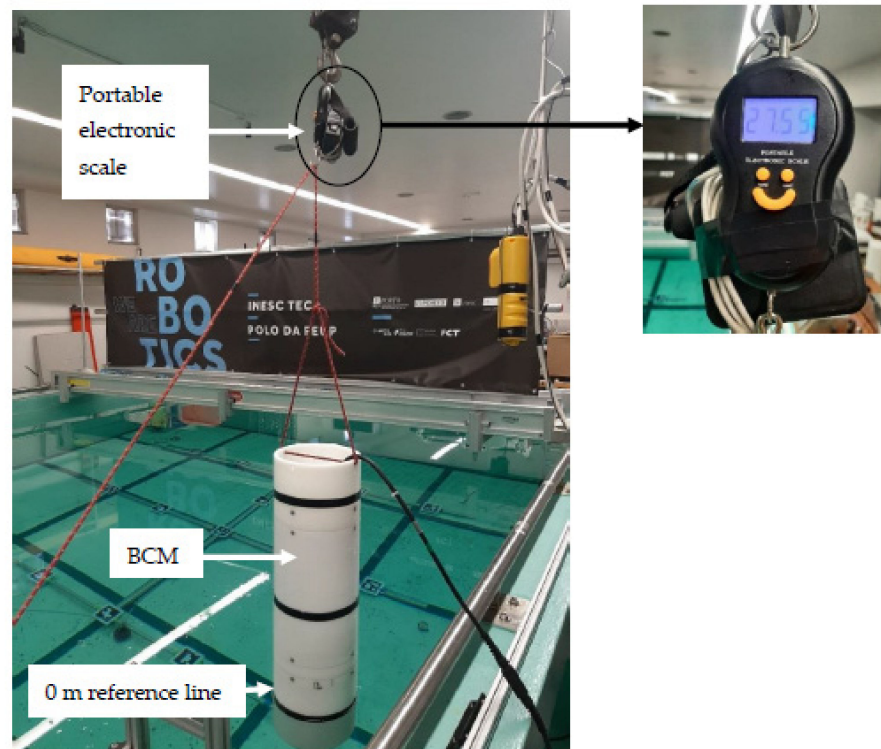


Figure 16. Picture of the experimental setup.

4.4.1. Buoyancy Measurements

Using the setup presented in Figure 16, the BCM weight was measured. The device weighs 22.2 kg out of water and without any flotation compensation, the device weighs 4.93 kg in water when the actuator is at its middle position. To measure the weight difference caused by moving the actuator, the portable scale was set to zero with the diaphragm cylinder retracted, and then the cylinder was extended. The stroke of the actuator was software limited to approximately 75% of the maximum stroke. This procedure was followed at depths from 0 to 1.5 m with a step of 0.5 m. Three retraction/extension cycles were conducted for each depth. Average results are shown in Figure 17.

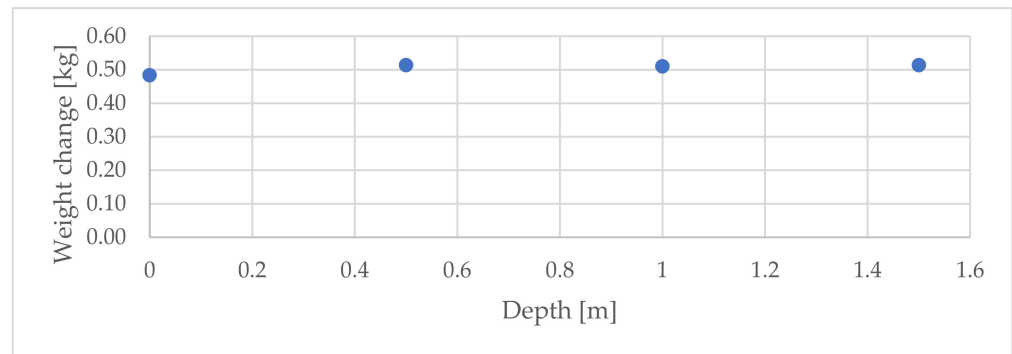


Figure 17. Buoyancy measurements at different depths (0 to 1.5 m with a 0.5 m step).

From these results, the useful weight change in this experiment is approximately 0.5 kg, corresponding to a volume change of approximately 500 cm^3 . Although there is not any significant influence of the pressure on the weight change, for 0 m depth, a slight reduction in the measured weight was noticed. This might be justified by the fact that the diaphragm was not fully stretched, given the low pressure difference at 0 m depth.

Figure 18 presents the difference between the calculated weight change using: (i) the displacement values read by the encoder, and (ii) the equivalent area of the rolling diaphragm cylinder provided by the manufacturer and the actual measured one. Slight differences of the order of tens of grams can be noticed. These differences are not considered relevant, given the resolution of the dynamometer and the uncertainty that might exist in the average rolling diaphragm area provided by the manufacturer. Finally, it should be noted that if the actuator had been set to use its full stroke, the expected weight change would be 0.66 kg in fresh water, corresponding to a maximum volume change of 660 cm^3 . Consequently, a good match between designed (700 cm^3) and actual volume change exists, differences being attributed to the uncertainty of the rolling diaphragm area provided by the manufacturer.

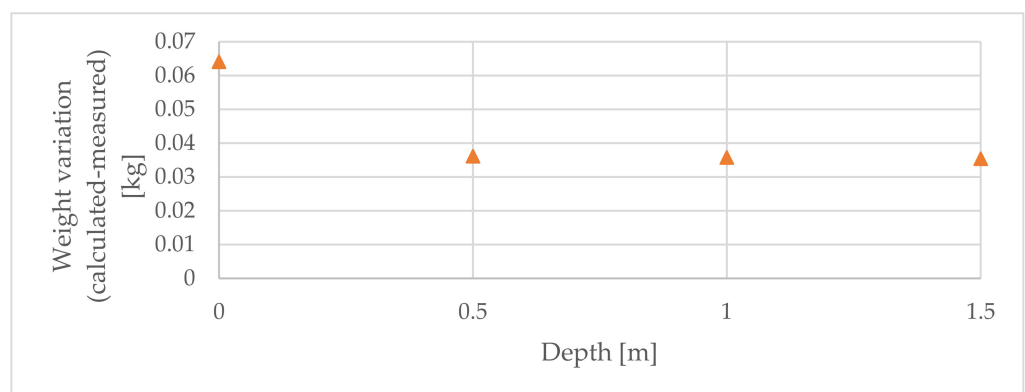


Figure 18. Buoyancy measurements at different depths (0 to 1.5 m with a 0.5 m step): comparison between measured and calculated values.

4.4.2. Power Consumption

The BCM average power consumption on water was measured at depths from 0 to 1.5 m with a step of 0.5 m, with the diaphragm cylinder moving at several traveling speeds between extended and retracted positions. The speeds were varied using three different duty cycles (DC): 20%, 50% and 80%, corresponding to the following average steady state velocities, respectively: 1.2 mm/s, 3 mm/s and 4.8 mm/s.

Results shown in Figure 19 indicate that:

1. An increase in the power required can be noticed for higher speeds. This is expected since: (i) the electric linear actuator is a DC motor, and for this type of voltage-controlled motors, higher steady state speeds require more voltage, and (ii) at higher speeds, the viscous friction forces are higher, thus the actuator must provide more force. Since the force provided by a DC motor is essentially dependent on the current provided to its coils, higher speeds require higher currents.
2. A slight increase in the power requirements can be noticed for higher depths, although results in this regard are not conclusive given the shallow pool available. This is expected since at higher depths the water pressure increases, thus requiring the actuator to exert more force for a given displacement.
3. There are lower power requirements when retracting than when extending. This can be justified by the fact that at higher depths the water pressure is higher, thus the actuator needs to perform less force when retracting and higher forces when extending. Consequently, less current is drawn from the power source when retracting than when extending. Even for lower depths, the vacuum inside the BCM creates a pressure difference which has an effect similar to the one caused by higher depths.

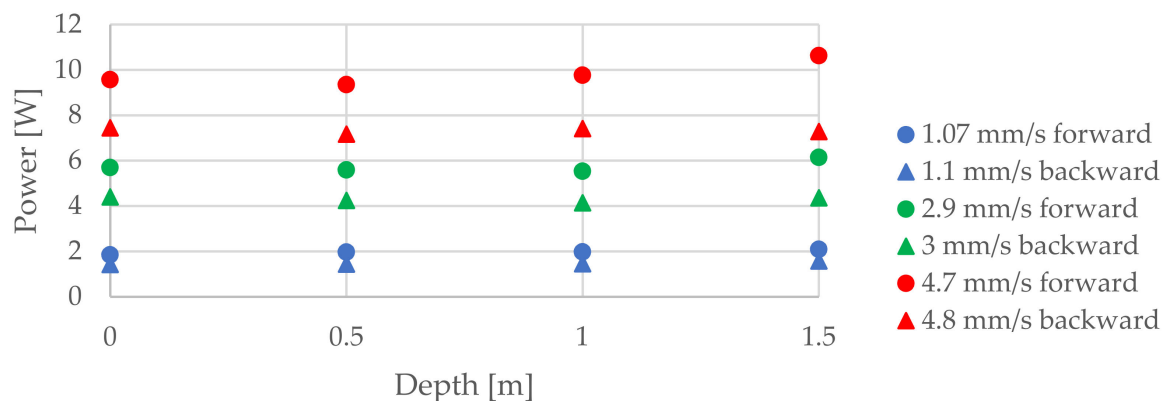


Figure 19. Power measurements at different depths and speeds.

By using the model developed in [6], a comparison between the actual average power values at the driver output and the ones predicted by the model, given the actual achieved velocities, was performed. Figure 20 shows this comparison. As can be seen, the model developed in [6] shows a reasonable accuracy for low speeds, although an increasing difference appears to exist for higher speeds. This difference might be justified by the increasing friction force caused at higher speeds by the actuator guidance and anti-rotation systems. Future work will therefore focus on including this friction effect on the model. It should nevertheless be emphasized that since the depths at which the BCM was tested in this study are very low, the actual power consumptions are correspondingly very low, so any power losses caused by friction effects have a significant impact. This is not the case, however, in normal operating conditions, where the error caused by friction is expected to be relatively much smaller. Future work will investigate this subject.

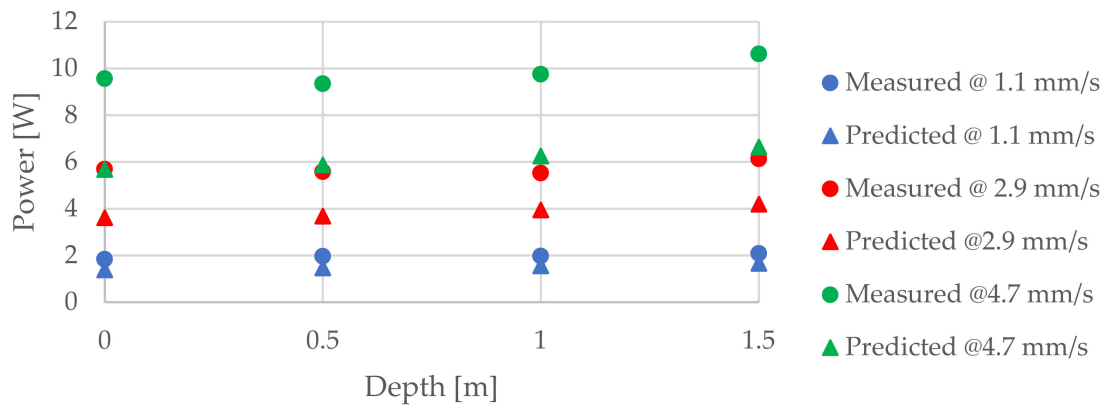


Figure 20. Power measurements at different depths when extending: comparison between measured and predicted values.

Finally, the energy spent in the above trials was computed. Results shown in Figure 21 present the energy measurements in backward and forward motions, and results in Figure 22 show a comparison between the measured and predicted values in forward motion. For the same depth, the higher the speed is, the higher is the energy required, but the energy percentage increase is smaller than the power percentage increase in similar conditions. In addition, when the actuator is retracting, the energy required does not seem to change significantly with depth, although a decrease would be expected. This might be justified by the fact that these tests were conducted at small depths, so a significant difference is not visible.

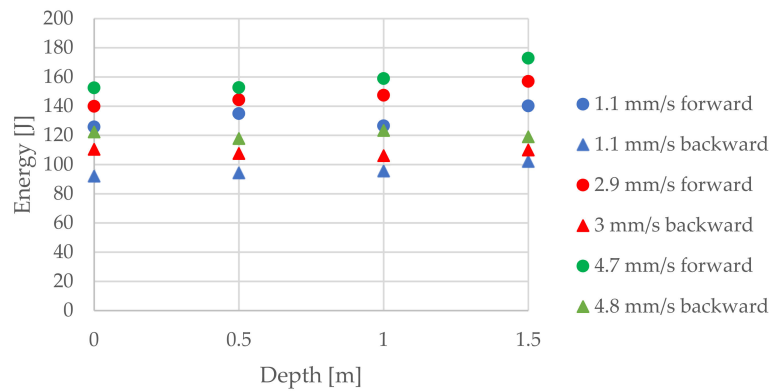


Figure 21. Energy measurements at different depths (0 m, 0.5 m, 1 m and 1.5 m) and speeds (DC = 20%, DC = 50%, DC = 80%).

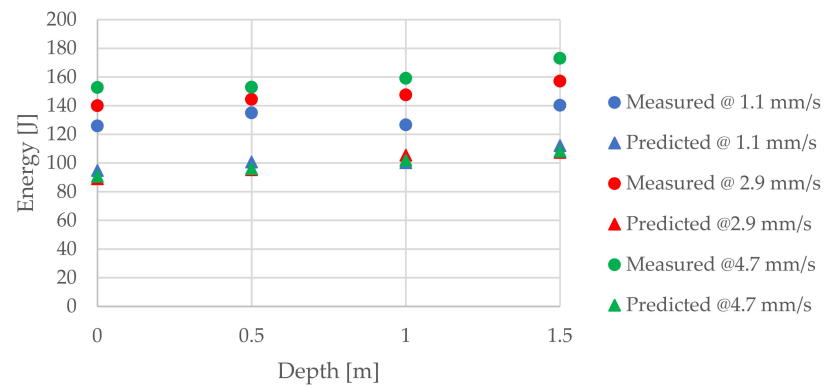


Figure 22. Predicted and measured values of energy at different depths (0 m, 0.5 m, 1 m and 1.5 m) and speeds (DC = 20%, DC = 50%, DC = 80%) when extending.

5. Conclusions

This work presented the development of a prototype of a buoyancy control module. A detailed analysis and justification of the choice of each individual component of the device, and of its mechanical design was provided. The developed buoyancy control module was experimentally tested in a pool for depths up to 1.5 m. These preliminary trials show that the prototype works as predicted, accomplishing the designed values of buoyancy and speeds. Experimental trials also allow a comparison between the power values predicted by the consumption model developed in a previous work by the authors and the ones that were measured. For low speeds, the model leads to errors of 20–30%, while for higher speeds the errors raise to values close to 40%. These significant prediction errors are probably caused by friction effects not accounted for in the previously developed model. It should be emphasized that this comparison was made for shallow waters, and since friction effects are not expected to increase significantly for higher depths, its relative weight should decrease, thus leading to lower relative prediction errors. Future work will focus on adding the friction effects to the developed model and conducting sea tests at higher depths. In addition, future work will pursue the implementation and testing of control strategies enabling the depth control of the module.

Author Contributions: Conceptualization, J.F.C., F.G.d.A. and N.A.C.; methodology, J.F.C., F.G.d.A. and N.A.C.; software, J.B.P.; investigation, J.F.C., F.G.d.A. and N.A.C.; writing—J.F.C.; writing—review and editing, J.F.C., J.B.P., F.G.d.A. and N.A.C. All authors have read and agreed to the published version of the manuscript.

Funding: This work was financially supported through contract LAETA—UIDB/50022/2020 by “Fundação para a Ciência e Tecnologia”, which the authors gratefully acknowledge.

Data Availability Statement: Not applicable.

Conflicts of Interest: The authors declare no conflict of interest.

References

1. Caffaz, A.; Caiti, A.; Casalino, G.; Turetta, A. The Hybrid Glider/AUV Folaga. *IEEE Robot. Autom. Mag.* **2010**, *17*, 31–44. [[CrossRef](#)]
2. Bellingham, J.G.; Zhang, Y.; Kerwin, J.; Erikson, J.; Hobson, B.; Kieft, B.; Godin, M.; McEwen, R.; Hoover, T.; Paul, J.; et al. Efficient propulsion for the Tethys long-range autonomous underwater vehicle. In Proceedings of the 2010 IEEE/OES Autonomous Underwater Vehicles, Monterey, CA, USA, 1–3 September 2010.
3. Hobson, B.W.; Bellingham, J.G.; Kieft, B.; McEwen, R.; Godin, M.; Zhang, Y. Tethys-class long range AUVs—extending the endurance of propeller-driven cruising AUVs from days to weeks. In Proceedings of the 2012 IEEE/OES Autonomous Underwater Vehicles (AUV), Southampton, UK, 24–27 September 2012.
4. Yoerger, D.; Curran, M.; Fujii, J.; German, C.; Gomez-Ibanez, D.; Govindarajan, A.; Howland, J.; Llopiz, J.; Wiebe, P.; Hobson, B.; et al. Mesobot: An Autonomous Underwater Vehicle for Tracking and Sampling Midwater Targets. In Proceedings of the 2018 IEEE/OES Autonomous Underwater Vehicle Workshop (AUV), Porto, Portugal, 6–9 November 2018.
5. Bachmayer, R.; Claus, B. Energy optimal depth control for long range underwater vehicles with applications to a hybrid underwater glider. *Auton. Robot.* **2016**, *40*, 1307–1320.
6. Falcão Carneiro, J.; Gomes de Almeida, F.; Pinto, J.B.; Cruz, N. Variable Buoyancy or Propeller-Based Systems for Hovering Capable Vehicles: An Energetic Comparison. *IEEE J. Ocean. Eng.* **2020**, *46*, 414–433. [[CrossRef](#)]
7. Wang, B.; Chen, Y.; Wu, Y.; Lin, Y.; Peng, S.; Liu, X.; Wu, S.; Liu, S.; Yi, J.; Polygerinos, P.; et al. An Underwater Glider with Muscle-Actuated Buoyancy Control and Caudal Fin Turning. *Machines* **2022**, *10*, 381. [[CrossRef](#)]
8. Ranganathan, T.; Pattery, J.; Thondiyath, A. Design and analysis of cable-connected metallic bellows as Variable Buoyancy Modules. In Proceedings of the 2015 IEEE Underwater Technology (UT), Chennai, India, 23–25 February 2015.
9. Ranganathan, T.; Singh, V.; Thondiyath, A. Theoretical and Experimental Investigations on the Design of a Hybrid Depth Controller for a Standalone Variable Buoyancy System—vBuoy. *IEEE J. Ocean. Eng.* **2018**, *45*, 414–429. [[CrossRef](#)]
10. Ranganathan, T.; Thondiyath, A. Design and Analysis of Cascaded Variable Buoyancy Systems for Selective Underwater Deployment. In Proceedings of the 13th International Conference on Informatics in Control, Automation and Robotics, Lisbon, Portugal, 29–31 July 2016.
11. Masmitjà, I.; González, J.; Gomáriz, S. Buoyancy model for Guanay II AUV. In Proceedings of the OCEANS 2014—TAIPEI, Taipei, Taiwan, 7–10 April 2014.
12. Skillings, B. *Buoyancy Engine Construction and Design for an Underwater Glider*, 1st ed.; National Research Council of Canada, Institute for Ocean Technology: Saba, The Netherlands, 2004.

13. Asakawa, K.; Hyakudome, T.; Ishihara, Y.; Nakamura, M. Development of an underwater glider for virtual mooring and its buoyancy engine. In Proceedings of the 2015 IEEE Underwater Technology (UT), Chennai, India, 23–25 February 2015.
14. Kobayashi, T.; Watanabe, K.; Ino, T.; Amaike, K.; Tachikawa, H.; Shikama, N.; Mizuno, K. New Buoyancy Engine for Autonomous Vehicles Observing Deeper Oceans. In Proceedings of the Twentieth (2010) International Offshore and Polar Engineering Conference, Beijing, China, 20–25 June 2010.
15. Woithe, H.; Chigirev, I.; Aragon, D.; Iqbal, M.; Shames, Y.; Glenn, S.; Schofield, O.; Seskar, I.; Kremer, U. Slocum Glider Energy Measurement and Simulation Infrastructure. In Proceedings of the Oceans 2010, Sydney, Australia, 24–27 May 2010.
16. Worall, M.; Jamieson, A.J.; Holford, A.; Neilson, R.D.; Player, M.; Bagley, P.M. A variable buoyancy system for deep ocean vehicles. In Proceedings of the OCEANS 2007—Europe, Aberdeen, UK, 18–21 June 2007.
17. Xia, Q.; Muhammad, G.; Chen, B.; Zhang, F.; Zhang, Z.; Zhang, S.; Yang, C. Investigation of Self-Driven Profiler with Buoyancy Adjusting System towards Ocean Thermal Energy. *Appl. Sci.* **2021**, *11*, 7086. [CrossRef]
18. Teledyne Webb Research. Slocum G2 Glider Operators Manual P/N 4343. Available online: http://gliderfs.coas.oregonstate.edu/gliderweb/docs/slocum_manuals/Slocum_G2_Glider_Operators_Manual.pdf (accessed on 26 July 2022).
19. Tiwari, B.K.; Sharma, R. Design and Analysis of a Variable Buoyancy System for Efficient Hovering Control of Underwater Vehicles with State Feedback Controller. *J. Mar. Sci. Eng.* **2020**, *8*, 263. [CrossRef]
20. Cruz, N.A.; Matos, A.C.; Ferreira, B.M. Modular building blocks for the development of AUVs—From MARES to TriMARES. In Proceedings of the 2013 IEEE International Underwater Technology Symposium (UT), Tokyo, Japan, 5–8 March 2013.
21. Cruz, N.A.; Matos, A.C. The MARES AUV, a Modular Autonomous Robot for Environment Sampling. In Proceedings of the OCEANS 2008, Quebec City, QC, Canada, 15–18 September 2008.
22. Polytechindustrial. Available online: <https://www.polytechindustrial.com/products/plastic-stock-shapes/acetal-copolymer> (accessed on 16 June 2022).